Design of MARCO, the new solenoidal detector magnet for the ePIC experiment at BNL

V. Calvelli, C. Berriaud, C. Genot, P. K. Ghoshal, S. Gopinath, F.P. Juster, V. Kleymenov, J.P. Lottin, L. Quettier, H. Reymond, M. Segreti, R. Sharma, D. Simon, F. Stacchi, E. Sun, R. Than, R. Wimmer, D. Young, E. Aschenauer, R. Ent, R. Rajput-Ghoshal

***Abstract*— MARCO is the new superconducting solenoid for ePIC, the general-purpose detector capable of delivering the full scientific scope of the Electron-Ion Collider at Brookhaven National Laboratory. This 3.84 m long solenoid, with a bore diameter of 2.84 m, will provide a magnetic field of 2.0 T at the center with a nominal current of 4 kA at 4.5 K, for a total stored energy of 45 MJ. Its conductor is a NbTi Rutherford in Copper Channel (RICC), specially designed to stand the high mechanical loads induced by the magnetic field. Its copper stabilizer will assure the protection in case of quench. The coils are wound into six layers inside a thin external mandrel in brass, with a triple role of mechanical reinforcement, cryogenic support for the thermosiphon circuit and quench-back propagator. With a cold mass average radial thickness of just 7 cm, the magnet fulfills all the criterions of transparency for the particles directed to the hadronic calorimeter forecast around the cryostat. In this paper, the design of MARCO is presented, with a specific focus on the magnetic and quench analysis.**

***Index Terms*—Superconducting magnets, solenoids, detector magnets, high-energy physics.**

I. INTRODUCTION

THE Electron-Ion Collider (Fig. 1) at Brookhaven National Laboratory will be the ultimate machine for nuclear physics and especially to study the nucleons. With its two highly polarized beams of 140 GeV for protons and ions and 18 GeV for electrons, this collider will reach a maximum luminosity of 10^{34} $cm^{-2}s^{-1}$ and it will provide a precision 3D imaging of protons and nuclei with the goals of solving the proton spin puzzle, reaching the limits of the quantum chromodynamics saturation and understanding the behavior of quarks and gluons [1]. To do so, a high performance detector (ePIC) is forecast [2] [3] [4] [5] (Fig. 2). The needed magnetic rigidity for secondary particles will be assured by a one-of-a-kind 2 T superconducting solenoid (Fig. 3), which design is the result of a joint effort between BNL, JLAB and CEA Saclay. MARCO (*Magnet with Renewed Coils*) presents some unusual design characteristics respect to other detector magnets [6] [7] [8] [9] [10]: the most important is its conductor, a NbTi Rutherford in Copper Channel (RICC), especially optimized to stand the forces during the cool-down and energization while providing a high enthalpy stability and a fast quench propagation. The coils of the magnet are wounded internally on a thin mandrel made of brass, which provides both a similar thermal retrain than the coil pack and, thanks to its mechanical properties, the needed rigidity without compromising the stringent criteria on the nuclear interaction length (magnet thickness) for secondary particles. The cool-down is guaranteed by a thermosiphon, which circuit is closed by a helium phase separator vessel placed outside the iron yoke and cryogenically connected to the main LHe circuit of the accelerator. The magnet is shifted of 100 mm towards the lepton side respect to the interaction point to better accommodate the sub-detectors. Such asymmetry has been considered while designing the iron yoke around, in order to minimize the magnetic forces acting on the magnet. In the following sections, the design of the overall magnet will be presented.

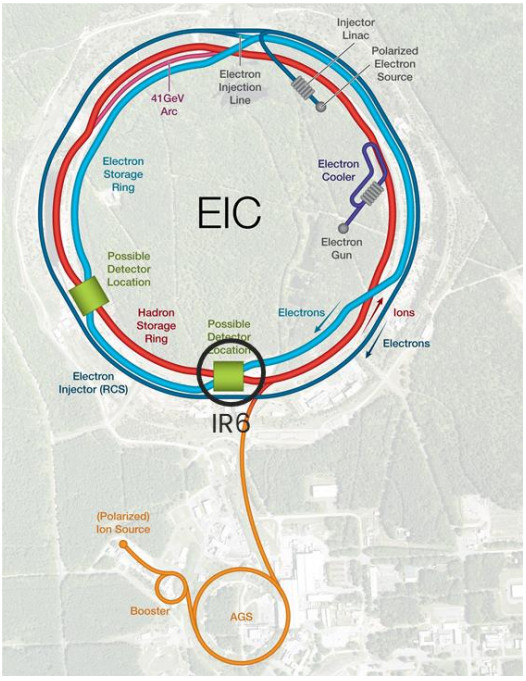

Fig. 1. Schematics of the Electron-Ion Collider at the Brookhaven National Laboratory. The ePIC detector will be installed in the Interaction Region 6 (IR6).

This paragraph of the first footnote will contain the date on which you submitted your paper for review, which is populated by IEEE. It is IEEE style to display support information, including sponsor and financial support

V. Calvelli, C. Berriaud, C. Genot, F.P. Juster, V. Kleymenov, J-P. Lottin, H. Reymond, L. Quettier, M. Segreti, D. Simon, F. Stacchi are with CEA-Saclay, France, F91191 Gif-sur-Yvette, France (e-mail: valerio.calvelli@cea.fr).

R. Ent, P. K. Ghoshal, S. Gopinath, E. Sun, D. Young, R Rajput-Ghoshal are all with Jefferson Lab, Newport News, VA, 23606 Phone: 757-269-6702

R. Sharma, R. Than, R. Wimmer, E. Aschenauer are with Brookhaven National Laboratory (BNL), Upton, NY (USA)

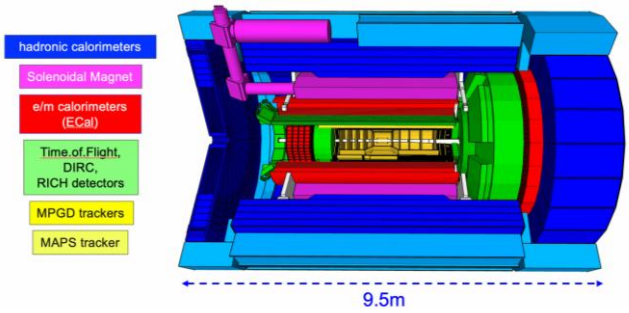

Fig. 2. Schematic overview of the ePIC detector with its main components (credits: the ePIC collaboration *[5]*)

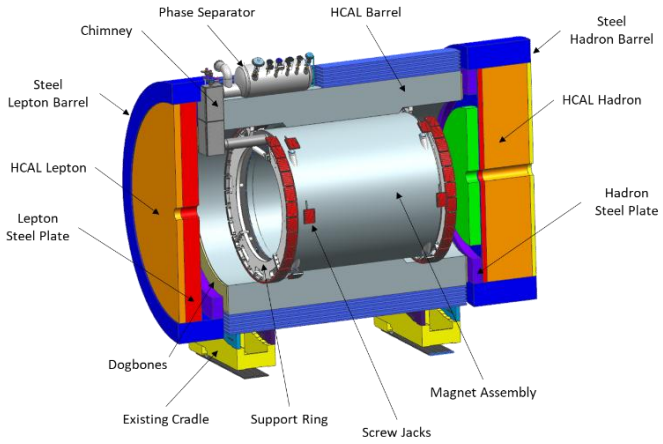

Fig. 3. Assembly overview of the MARCO magnet inside its iron yoke. The iron yoke is divided in three separate sections, respectively Lepton, Barrel and Hadron, made of several components, including some hadronic calorimeters. Their names indicate the sides from which the particles beams come.

II. Requirements

The requirements for MARCO are described in Table 1:

Table 1
MARCO Requirements

Parameter	Value	Unit
Nominal central field at IP	2.0	T
Operating field range	0.5 ÷ 2.0	T
Magnetic field polarity	Bipolar	
Coil length	3492	mm
Warm bore diameter	2840	mm
Cryostat length	< 3850	mm
Cryostat outer diameter	< 3540	mm
Yoke diameter	≤ 6500	mm
Axial yoke length	≤ 9500	mm
Field uniformity in the Flat Field area	12.5 %	
Integrated fringe field on RCS	< 0.007	Tm
Fringe field on IR magnets	< 10	G
Projectivity in RICH area	< 10	T/Amm²
Nuclear interaction length	< 0.5	g/cm²
Charging voltage	< 10	V
Fast discharge voltage (max)	±500	V
Quench hot spot temperature	< 150	K
Temperature margin	> 1.5	K
Current margin (I/I_{SSL})	< 30%	
Operating temperature	4.5	K

Regarding the magnetic performances demanded, there are three zones of main interest:

A. The Flat Field area

Described as cylinder of radius 800 mm for a total length of 2000 mm, centered on the interaction point IP (Fig. 4). For this area, the requirement is to have a field uniformity defined as (1):

$$Field\ uniformity = 100 \cdot \frac{dB}{B_{center}} \quad (1)$$

Where:
$dB = B_{max} - B_{min}$ in the area of interest and
B_{center} the magnetic field in the center of the magnet

B. The RICH (Ring Imaging Cherenkov) area

In order to maximize the Ring Imaging Cherenkov detector (RICH) performances based on the gas radiator, it is critical to minimize the bending of the tracks in the volume of the gas radiator, for this one need to shape the field such that it is parallel to the different scattering angles of particles covered by the RICH. The RICH area extends from z=+1800 mm to +2800 mm with the shape of a truncated cone (Fig. 5). The projectivity in this region should be less than 10T/Amm² or less than 0.1 mrad @30GeV/c for a proton. The projectivity can be calculated as (2):

$$Proj = \frac{1}{\Omega}\int_{\Omega} \frac{|B_r| - \left|\frac{r}{z}B_z\right|}{J_e} d\Omega \quad (2)$$

Where Ω is the gas volume of the detector, B_r and B_z are respectively the radial and the axial component of the magnetic, J_e the engineering current density of the magnet.

C. The Interaction Region (IR) magnets and Rapid Cycling Synchrotron (RCS)

The detector solenoid has neighboring Interaction Region (IR) magnets, the so-called B0ApF and Q1ApR, which extends from z = 7.4 m to 8 m and z = -5.3 m to -7.1 m respectively (Fig. 6). In order to not perturb the particle beams, the fringe field produced by the solenoid on these magnets needs to be less than 10 G. The Rapid Cycling Synchrotron (RCS) at the time of the design was radially at 3352 mm from the magnet central axis and stray field requirement there is <0.007 Tm. Although it has been decided to move it outside the tunnel after the completion of the design, we are waiting for the stray field requirement to be updated by BNL. In order to be conservative, we keep it in consideration for our design.

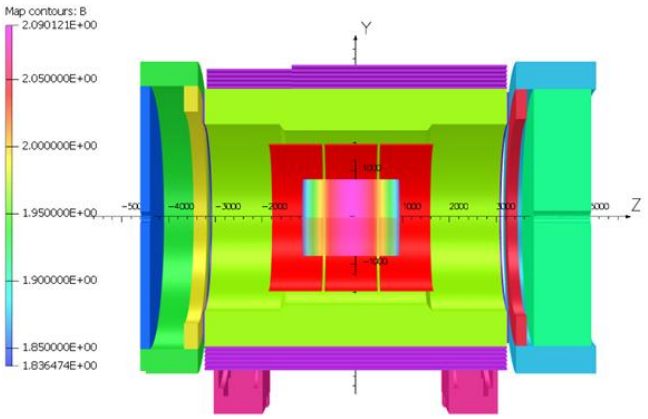

Fig. 4. The Flat Field area in the legend colors. The legend reports the magnetic field on this surface. Only the ferromagnetic parts and the coils are represented.

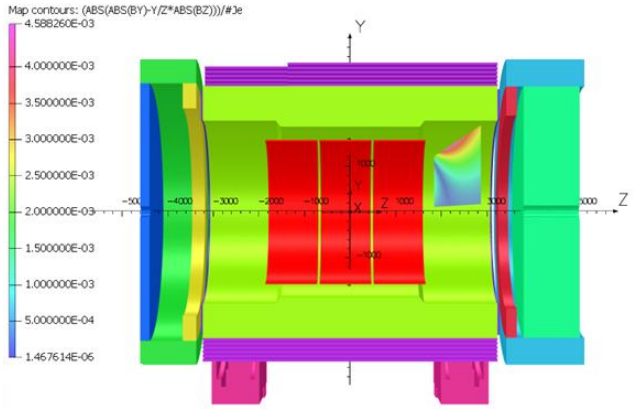

Fig. 5. Cross-section of the RICH area the legend colors. The legend reports the integrand of the formula (2) on the surface. Only the ferromagnetic parts and the coils are represented.

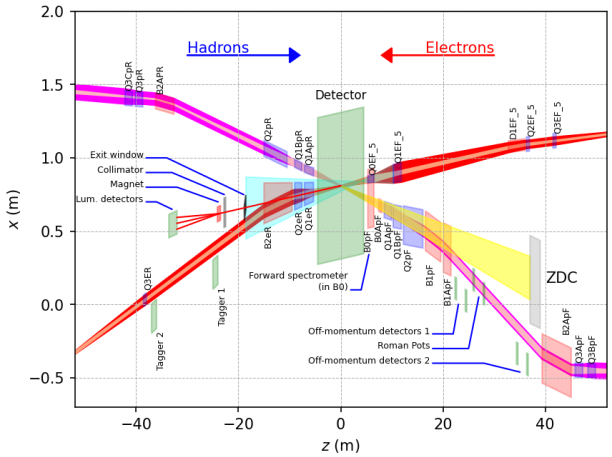

Fig. 6. Interaction region layout, with the location of the IR magnets B0ApF and Q1ApR.

III. Geometry and Materials of the Yoke

The magnetic flux generated by the superconducting coils is returned via three distinct sections of yoke: the Barrel Yoke, the Lepton Yoke and the Hadron Yoke (Fig. 3). Their geometry has been defined through an optimization process which includes both the experimental constraints and the requirements for the fringe field.

A. Barrel Yoke

The Barrel Yoke consists of the HCal Barrel Calorimeter and the Steel Barrel Yoke. The HCal Barrel Calorimeter is made with 32 assembled sectors composed by 10 rows of 8 mm scintillators tiles (24 tiles per row), tilted with an angle of 12°. In each sector, 26.1 mm x 42.4 mm x 6300 mm tapered 1020 steel plates are piled up and used to separate each scintillator tile. The total fraction of steel in the volume is 70%. Dogbones made by the same steel enclose the calorimeter. Their fraction of steel in the volume is 66%. The Steel Barrel Yoke is made by 6 concentric rings of steel 1020, 50 mm thick, 6300 mm long, surrounding the HCal Barrel Calorimeter. Each ring is separated from the other by 40 mm. A specific volume is dedicated to the installation of the He phase separator, from which all the cryogenics circuits inside the cold mass are supplied. The Steel Barrel Yoke main purpose is to reduce the stray field.

B. Hadron Yoke

The Hadron Yoke consists of the HCal Hadron Calorimeter, the Steel Barrel Hadron Yoke and the HCal Hadron Oculus. Its name is given by the convention on the direction of the beams. In this case, the hadron beam is the one exiting the detector. The HCal Hadron Calorimeter is made by 70 pieces of 4 mm thick scintillator tiles, 10 pieces of 16 mm thick tungsten plates and 60 pieces of 16 mm thick steel 1020 plates. The average fraction of steel 1020 in the total volume is 75%. The Steel Barrel Hadron Yoke as well as the HCal Hadron Oculus are two structures in steel 1020 surrounding the calorimeter and returning the magnetic flux.

C. Lepton Yoke

The Lepton Yoke is composed by the HCal Lepton Calorimeter, the Steel Barrel Lepton Yoke and the HCal Lepton Oculus. Its name is given by the convention on the direction of the beams. In this case, the electrons beam is the one exiting the detector. The HCal Lepton Calorimeter is made by 50 pieces of 4 mm thick scintillator tiles, 10 pieces of 16 mm thick tungsten plates and 60 pieces of 16 mm thick low carbon steel (Steel 1020) plates. The average fraction of steel 1020 in the total volume is 75%. The Steel Barrel Lepton Yoke as well as the HCal Lepton Oculus are two structures in steel 1020 surrounding the calorimeter and returning the magnetic flux. The steel 1020 BH curve is shown in Fig. 7.

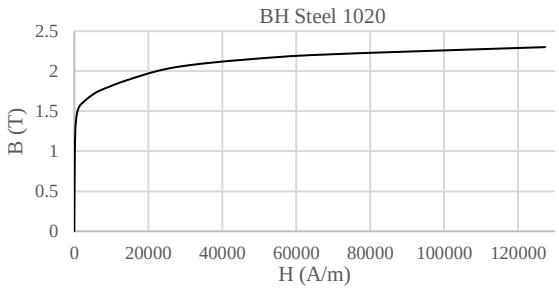

Fig. 7. BH curve of Steel 1020

For all the electro-magnetic simulations, the envelope of each component of the yoke has been considered, and for each volume a dilution percentage corresponding to the average fraction of steel present has been taken into account.

IV. Description of the Magnet

The solenoid is made of three modules with three identical superconducting coils wounded internally on a mandrel in brass comprising 70% of copper and 30% of zinc (brass 70-30). The coils are indirectly cooled using a thermosiphon (Fig. 8). All the cryogenics circuits are connected to a LHe phase separator, connected itself to the main cryogenics circuit of the accelerator. The connection is made through a chimney, where the current leads are also placed.

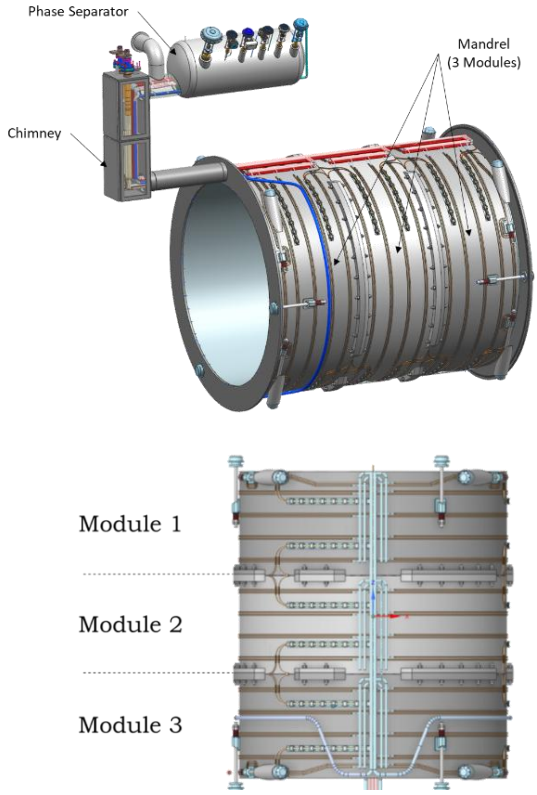

Fig. 8. MARCO cold mass layout inside the cryostat (top) and its three modules (bottom). Module 3 is the one closer to the chimney, and on the lepton side. Module 1 is on the hadron side

For each module, 6 single layers of RICC conductor are wound internally to a mandrel, for a total number of turns per layer varying between 92 and 93, according to the conductor exits. Modules are named MOD1, MOD2 and MOD3. The total number of turns per module is 556. Layers are named L1, L2, L3, L4, L5, L6 with L1 being the innermost and L6 the outermost. Each layer is separated by an inter-layer fiber glass insulation of 2 layers of 0.2 mm to achieve a good electrical insulation after winding and to prevent the conductor damages. The coil pack is separated from the mandrel by 1 mm of ground insulation, the same value as CMS solenoid [8], to prevent electrical short-circuits, to protect the conductor insulation during winding, and to facilitate the impregnation keeping a good thermal coupling for cool-down and quench-back. A schematic cross-section of the coil pack is shown in Fig. 9.

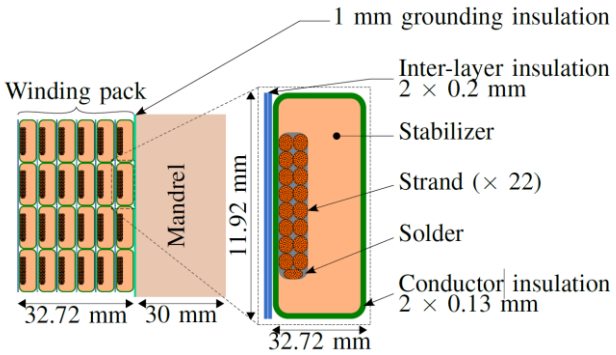

Fig. 9. On the left, schematic cross-section of the coil pack and mandrel, with the thickness of each item. On the right, the schematic cross-section of the RICC NbTi conductor chosen, with the dimensions of each element.

On the inner side of the coil pack, the impregnation should provide an average thickness of G10 of 2 mm.
The geometric specifications and dimensions of MARCO solenoid are reported in Table 2:

TABLE 2
MARCO GEOMETRIC SPECIFICATIONS

Parameter	Value	Unit
Bore radius	1420	mm
Cryostat outer radius	1770	mm
Cryostat axial length	3850	mm
Mandrel Length (300K)	3620	mm
Mandrel Length (4K)	3608	mm
Number of Modules	3	
External Modules (MOD1) (MOD3) Length (300K)	1228	mm
Central Module (MOD 2) Length (300K)	1164	mm
Coils Inner Radius (300K)	1509.5	mm
Coil Inner Radius (4K)	1502.5	mm
Coils Thickness	32.7	mm
Coils Outer Radius (300K)	1542.2	mm
Ground Insulation Thickness	1	mm
Mandrel Inner Radius	1543.2	mm
Mandrel Thickness	30	mm
Mandrel Outer Radius (300K) without Flanges	1573.2	mm
Mandrel Outer Radius (4K) without Flanges	1566.2	mm
Mandrel Outer Radius (300K) including Flanges	1646.1	mm
Mandrel Outer Radius (4K) including Flanges	1639.1	mm
Number of Layers per Module	6	
Number of Turns per Module	556	

The electric scheme for the solenoid is shown in Fig. 10. Each layer is made by winding one conductor unit length (~1 km long), and all the layers are connected in series with conductor splices outside the mandrel.

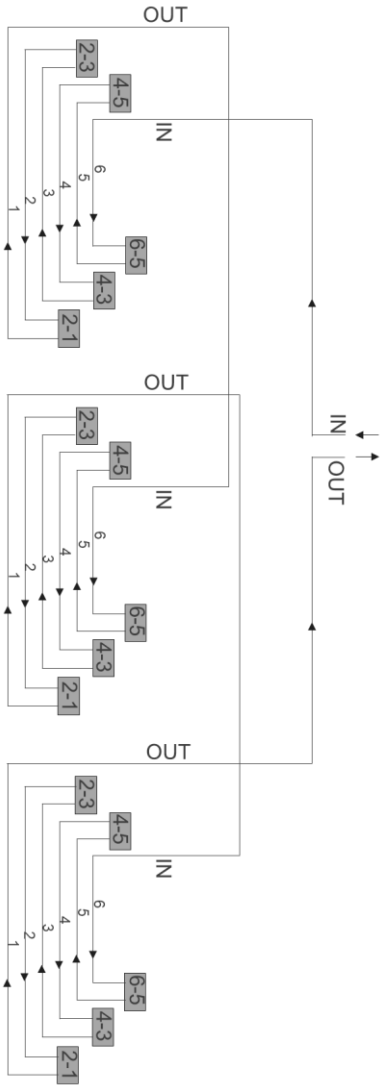

Fig. 10. Electric schematic of MARCO Solenoid.

Conductor exits are positioned at approximately 120° on the mandrel as shown in Fig. 11:

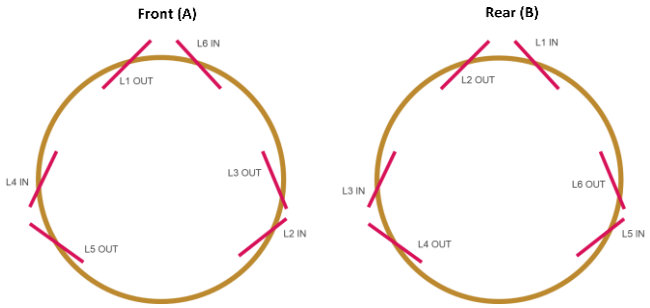

Fig. 11. Conductor entrance and exit schematics for each module.

Such arrangement preserves the number of turns. The extremities (front/rear) of each coil pack have in total 5 turns over 6. The exits will be made with grooves cut in the mandrel. Each groove will be:

a) Thick enough to double the conductor in order to increase the stability and to insulate it with G10 fillers and fiberglass insulation (Fig. 12);
b) Tangent to the outer diameter of each terminal with a 1 mm G10 plate between the splice and the mandrel;
c) Separated with a distance larger than two times of the hard-way radius of the conductor (2 x 120 mm).

A schematic of the grooves' arrangement is shown in Fig. 12 and Fig. 13. Splices between doubled conductors are thermalized thanks to a series of copper plates connected to the mandrel [10], itself cooled down by the thermosiphon.

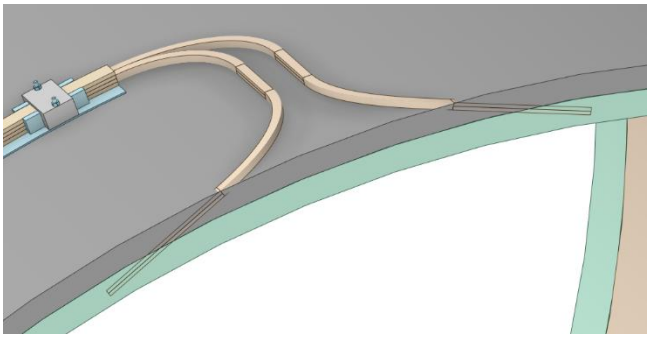

Fig. 12. Design of the splices exits from the mandrel.

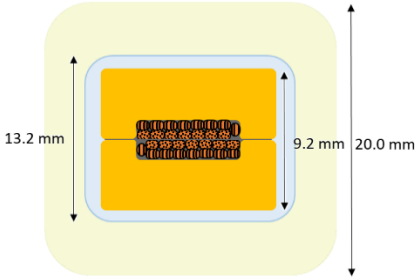

Fig. 13. Schematic cross-section of the splice to be placed inside the groove.

In order to fulfill the requirements in Table 1, the mandrel is longer than the coil for each module. The extra length is equal to 24.84 mm (2x11.92 mm [2 turns] plus 1 mm for tolerances), which gives a separation of 55.5 mm between each coil. This gap will be filled with G10 wedges, which will be glue to the mandrel, plus a 3 mm insulation between each module to take care of the tolerances of manufacturing, positioning and tolerance stack up (Fig. 14).

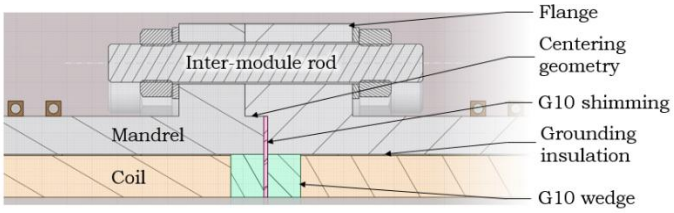

Fig. 14. Schematics of the geometry at the interface between each coil.

Each module is impregnated independently and bolted together through flanges. Flanges are not continuous on the entire circumference of the mandrel in order to let the thermosiphon pipes, the conductor splices and wire sensors all the space required. On the two outer modules, 4 radial and 3 axial tie-rods in Ti_6Al_4V are present to sustain the mass of the magnet and the efforts during the cool-down and the energization. A schematic description of the tie-rods is shown in Fig. 15. A general scheme

of the magnet assembly inside the cryostat is shown in Fig. 16. In the same figure, the two thermosiphon manifolds (the main and the spare) with the respective supply lines and heat exchangers are showed. The specifications of the thermosiphons are detailed in paragraph IX. The cold mass is placed inside a cylindrical vacuum vessel made from Aluminum alloy 6061 tempered T6 (Al6061-T6) (Fig. 17), with a thickness on the inner and outer shell of respectively 14 mm and 25 mm. The two shells joint together through flanges 40 mm thick. Inside the cryostat, a thermal shield made from Al3003 with 3 × 4 internal panels and 3 × 4 outer panels are located. The thermal shield is cooled by 3 circuits in parallel, cooling the internal panels first. Between the vacuum vessel and the outer shield, there are 30 layers of MLI; while between the coil and the internal shield, there are 10 layers of MLI to guarantee the superinsulation.

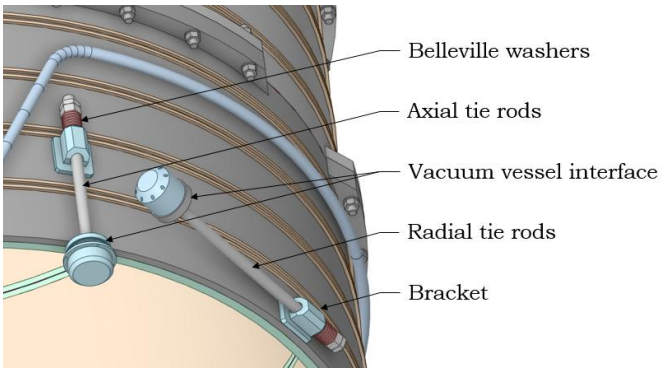

Fig. 15. Schematics of the tie-rods geometry

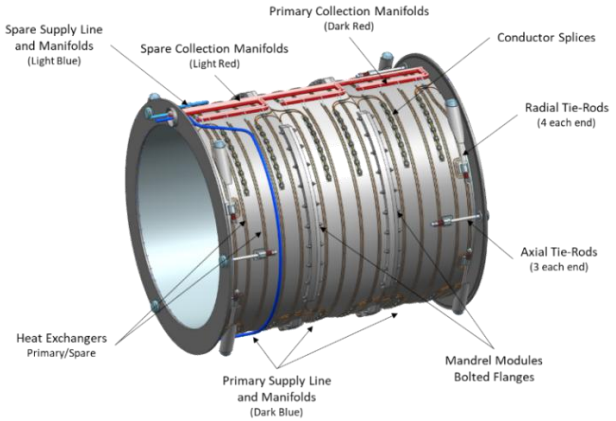

Fig. 16. Magnet assembly inside the cryostat.

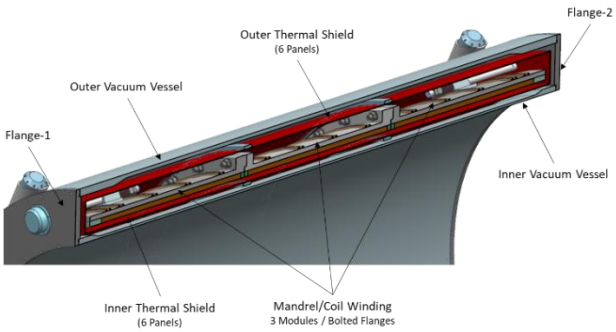

Fig. 17. Schematics of the cryostat with the magnet inside.

The full list of the main materials is reported in Table 3:

TABLE 3
MARCO MATERIALS

Component	Radial thickness (mm)	Material	Nuclear interaction length [11] (g/cm^{-2})
Inner vacuum vessel	14	Al6061	107.2
Inner thermal shield	5	Al3003	107.2
Inner G10	2	G10	78.4
Coil	33.7	14% insulation 80% Cu 6% NbTi	insulation: 78.4 Cu: 137.3 NbTi: 140.25
Mandrel	30	Brass 7030	137.7
Outer thermal shield	5	Al3003	107.2
Outer vacuum vessel	25	Al6061	107.2

The Thickness/Nuclear interaction length weighted according to the material densities for MARCO is 0.495.

V. MAGNETIC DESIGN

A. Nominal Design

The magnetic design has been performed using OPERA [12], with 2D and 3D finite element models. Given the high level of symmetry in the magnet, both models give the same results in terms of magnetic field and magnetic performances. The 2D axisymmetric model is used to compute the magnetic field turn-by-turn and to determine the magnetic field peak on the cable (Fig. 18), while the 3D model (Fig. 4, Fig. 5, Fig. 19) is to take into account the role of the mandrel during the ramp-up/ramp-down and the quench, as well as the effect of the cradles and the phase separator.

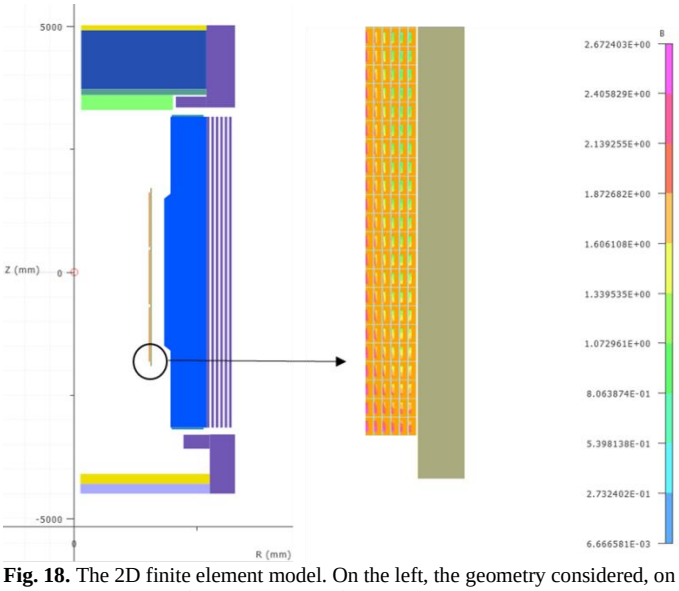

Fig. 18. The 2D finite element model. On the left, the geometry considered, on the right the results for the magnetic field peak on the cable, located at the extremity of module 1.

Three are the magnetic fields at the interaction point IP that are relevant for physics: 1.5T (minimal field), 1.7T (nominal field for the ePIC detector [2]) and 2.0T (ultimate field for the ePIC

detector, nominal field for the magnet). The nominal magnet performances for each case are reported in Table 4:

TABLE 4
NOMINAL MAGNET PERFORMANCES

Parameter	B_{IP} = 1.5 T	B_{IP} = 1.7 T	B_{IP} = 2.0 T	Units
Current	2942	3335	3924	A
B_{IP}	1.505	1.706	2.000	T
B_{peak}	2.003	2.271	2.672	T
Energy	25.440	32.689	45.008	MJ
L_{coils}	5.847	5.847	5.846	H
$L_{mandrel}$	$2.347 \cdot 10^{-6}$			H
$M_{coils\text{-}mandrel}$	$3.570 \cdot 10^{-3}$			H
F_z	-23.8	-29.2	-32.2	kN

It is important to notice that the primary inductance of the magnet L_{coils} is essentially constant. The iron yoke plays a negligible role on the performances of the magnet since it does not saturate (Fig. 19). The same trend is observed on the secondary inductance $L_{mandrel}$. The total axial force acting on the magnet due to its interaction with the yoke is monotone respect to the current (it increases as the current increases) and it points always in the lepton direction (-z). The maximum value of the force is 32.2 kN, and it is negligible respect to the forces the magnet can stand during transportations (see paragraph VI). The magnet is well balanced respect to the yoke in terms of electromagnetic interaction.

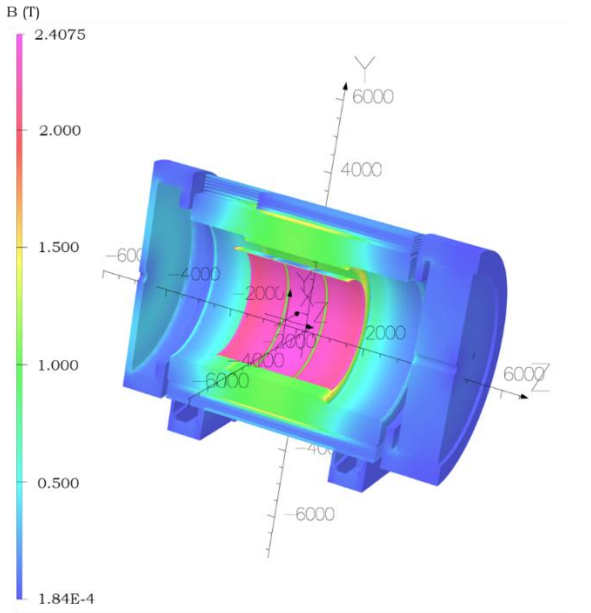

Fig. 19. 3D magnetic field on the coil and yoke as calculated in the 3D OPERA model for the 2.0 T nominal case. The difference on the magnetic field peak in 2D and 3D is because in 3D the contribution of the self-field of the cable cannot be take into account.

The magnetic performances are reported in Table 5:

TABLE 5
NOMINAL MAGNETIC PERFORMANCES AT B_{IP} = 2.0 T

Parameter	Value	Requirements	Unit
Field uniformity	12.5%	12.5%	
Projectivity	3.28	< 10	T/Amm^2
B_{RCS}	0.035	<0.007	Tm
B_{B0ApF}	15.4	<10	G
B_{Q1ApR}	10.9	<10	G

The design today respects the requirements for the field uniformity and the projectivity, however the fringe field is still too high. Since the values for the fringe field are in the order of 1 mT, a series of local shields around the magnets are under investigation. Since the RCS will be placed outside the tunnel, the requirement on the RCS will change and therefore it is not considered as major obstacle. Since these are local solutions on components external to the detector, they are not part of the design of the MARCO magnets.

B. Fault scenarios

In order to assess the robustness of the design, different fault scenarios respect to the nominal design have been considered:

B1. Axial misalignments and tolerances

The impact of axial misalignments and fabrication tolerances with respect to the nominal position and dimensions of the magnet has been studied in the 2D model using Monte Carlo simulations. The following hypotheses have been considered. Respect to the nominal position:

- Every module can be displaced along Z with a gaussian distribution $G(\mu, \sigma) = G(0.0, 5.0\ mm)$;
- Every module can have a different inner radius modeled with a gaussian distribution $G(\mu, \sigma) = G(1502.5\ mm, 5.0\ mm)$;
- Every module can have a different angle (as if the mandrel has a conical shape and not cylindrical) modeled with a gaussian distribution $G(\mu, \sigma) = G(0.0, 0.03\ deg)$;
- The cold mass can be displaced along Z with a gaussian distribution $G(\mu, \sigma) = G(0.0, 10.0\ mm)$;
- 1000 simulations are considered for this study.

Such values for each standard deviations have been considered according to the maximum tolerance and misalignments that will be imposed to the manufacturer and during the installation. When considering 3σ, each tolerance corresponds to around 1% of the corresponding parameter.

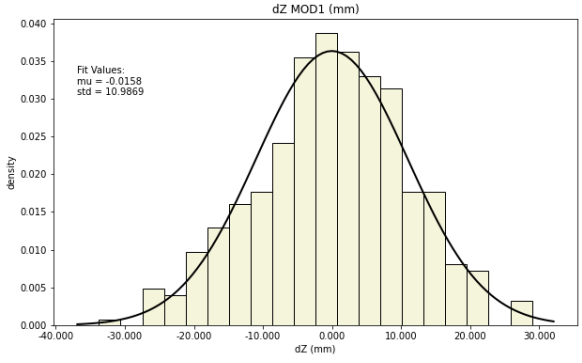

Fig. 20. Amplitude of the possible misalignments for the MOD1 with respect to the nominal position.

As a result, 99.7% of modules misalignments with respect to the nominal position are less than 33 mm (1% of the length of the cold mass), with a maximum of 40 mm (Fig. 20 as example for MOD1). If one assumes that the mandrel may have a conical

shape due to the fabrication process, the maximum admissible angle of the cone is 0.1 rad (5.73°), corresponding to a tolerance of 0.3% on the inner radius.
Table 6 summarizes the negligible impact on the magnet performances even in case of large displacements/tolerances:

TABLE 6
IMPACT OF AXIAL MISALIGNMENTS AND TOLERANCES

Parameter	Value	Unit
Δ B_{IP}	±10	mT
Δ Energy	±0.231	MJ
Δ F_z	+14.4/-50.4	kN
Δ Field uniformity	±1%	
Δ B_{RCS}	1.9E-4	Tm
Δ B_{B0ApF}	±0.2	G
Δ B_{Q1ApR}	±0.15	G

It is important to notice that the total axial force F_z can change of direction respect to the nominal design. Tie-rods have been designed accordingly to stand these changes.

B2. Radial misalignments

The impact of radial misalignments with respect to the nominal position of the magnet has been studied in the 3D model due to the breakdown of symmetry these misalignments create. Due to the complexity of the simulations and especially their computation time, a maximum misplacement was studied, with the following hypotheses:

- Every module can be displaced along Y with a maximum displacement of 5.0 mm.
- The cold mass can be displaced along Y with a maximum displacement of 5.0 mm.

The most meaningful results are reported from Table 7 to Table 10. As well as the axial misalignments, the radial displacements of the modules or the cold mass have a negligible impact on the field quality and B_{IP}: for the magnetic field at center, the maximum variation is ± 1mT, while for the field quality we expect an impact on homogeneity less than 0.1%. For what concerns the forces acting on the magnet, they are of the order of the weight of the magnet itself and lower than the transportation loads. Therefore, a tolerance in the position of the coils of 5 mm is acceptable.

TABLE 7
IMPACT OF RADIAL MISALIGNMENTS - COLD MASS

Parameter	MOD1	MOD2	MOD3	MAGNET	Unit
Δ y				± 5	mm
Δ F_y	±12.3	±14.5	± 15.3	± 42.2	kN
Δ F_z				-32.5	kN

TABLE 8
IMPACT OF RADIAL MISALIGNMENTS - MODULE 1

Parameter	MOD1	MOD2	MOD3	MAGNET	Unit
Δ y	± 5				mm
Δ F_y	-0.5 +0.7	-39.2 39.4	25.3 -24.9	-14.5 15.1	kN
Δ F_z				-32.2	kN

TABLE 9
IMPACT OF RADIAL MISALIGNMENTS - MODULE 2

Parameter	MOD1	MOD2	MOD3	MAGNET	Unit
Δ y		± 5			mm
Δ F_y	64.4 -64.3	-39.7 39.6	-14.6 14.6	-14.7 14.7	kN
Δ F_z				-32.5	kN

TABLE 10
IMPACT OF RADIAL MISALIGNMENTS - MODULE 3

Parameter	MOD1	MOD2	MOD3	MAGNET	Unit
Δ y			± 5		mm
Δ F_y	27.8 -27.6	-39.4 39.3	-0.9 0.9	-12.3 12.4	kN
Δ F_z				-32.4	kN

B3. Impact of one missing layer

The impact of one missing layer in a module due to an electrical shortcut can be different depending on which module is concerned. The results are reported in Table 11:

TABLE 11
IMPACT OF ONE MISSING LAYER

Parameter	MOD1	MOD2	MOD3	MAGNET	Unit
Δ B_{IP}	1.923	1.838	1.906	2.000	T
Δ Energy	40.610	39.679	40.590		MJ
Δ F_z	-90.8	-39.4	+42.3	-23.3	kN
Δ Uniformity	19.3%	8.5%	19.3%	12.5%	
Δ B_{RCS}	0.040	0.035	0.030	0.035	Tm
Δ B_{B0ApF}	13.7	14.6	14.6	15.3	G
Δ B_{Q1ApR}	10.5	10.5	9.7	10.9	G

In case that one layer is missing in MOD1 or MOD3, the operation of the magnet is compromised due to the high non-homogeneity of the magnetic field. Otherwise, the magnet can still respect the requirements if only MOD2 has one missing layer. The detail operating margins need to be calculated in the event of a missing layer, and based on which the operating limits will must be set accordingly for all materials.

B4. Impact of the magnetic permeability of the yoke

A variation of ±10% of the BH curve in Fig. 7 shows that the variation of the main parameters is negligible (less than 1 part per 10^4 for each).

B5. Impact of the misalignments of the yoke

The impact of axial misalignments, fabrication tolerances with respect to the nominal position, and dimensions of the yoke has been studied in the 2D model using Monte Carlo simulations. The following hypotheses have been considered:

- Every yoke element can be displaced along Z with a gaussian distribution $G(\mu, \sigma) = G(0.0, 5.0\ mm)$ with respect to the nominal position.
- Every yoke can have a different inner/outer radius modeled with a gaussian distribution $G(\mu, \sigma) = G(0.0, 5.0\ mm)$ with respect to the nominal position.
- 1000 simulations are considered for this study.

Only the fringe field was analyzed for this study.
The impact of yoke misalignments is negligible with respect to the fringe field. When considering misalignments / tolerances

of 15 mm (the maximum displacement observed in the Monte Carlo simulations), the maximum variation of the fringe field is:

- $\Delta B_{B0ApF} = \pm 1.5$ G
- $\Delta B_{Q1ApR} = \pm 1.2$ G
- $\Delta B_{RCS} = \pm 3 \cdot 10^{-5}$ Tm

B6. Mitigation strategy

Thanks to the fault scenario analysis, the magnet is expected to respect the requirements design with an uncertainty of ± 1% in terms of field homogeneity and of 10 mT in terms of field at center due to tolerances and misalignments. These uncertainties may have an impact on the physics and evaluations are ongoings. However, the magnet can provide 2.0 T as ultimate field (17.6% more magnetic flux respect to the nominal operative field of 1.7 T for the ePIC detector). This should largely compensate the impact of the uncertainties of the field homogeneity. The reason why we chose to increase the magnetic field respect to improve the homogeneity is due to the complexity of the design and a benefits/risks analysis: having limited space, in order to inprove the homogeneity we should have or using grading and designing two conductors (with extra cost for production and integration) or remove one layer in MOD2, reducing the ultimate field at center and complexifying both the electrical joints scheme and the module design, which would have needed an extra layer of material in any case in order to correctly stand the force distribution inside the coil without decreasing the mechanical performances of the magnet.

VI. Conductor Design

The conductor chosen for MARCO is a NbTi Rutherford In Copper Channel (RICC). Its design follows the Iseult Conductor [13] [14], designed by CEA and Luvata and currently used in the Iseult 11.7T MRI magnet [15]. A complete

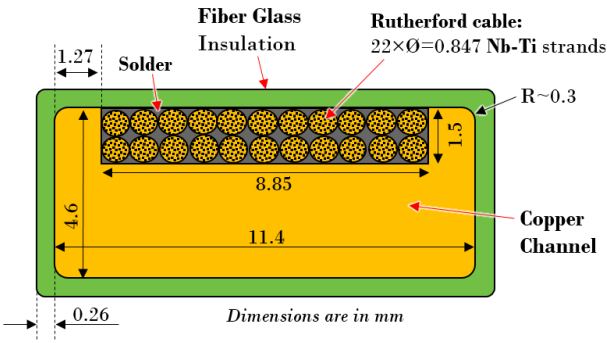

Fig. 21. Cross-section of the RICC conductor designed for MARCO solenoidal magnet. The insulation thickness is made from fiberglass and consists of 2×0.13 mm 50% overlap tape. The Rutherford cable is soldered into the copper channel.

description of the conductor and the choices made for its definition can be found in the dedicated paper [10]. A schematic cross-section of the conductor is shown in Fig. 9 and Fig. 21.
The main specifications of the conductor taken into account to perform the design are listed in Table 12:

Table 12
Main specifications of the MARCO RICC Conductor

	Parameter	Value	Unit
Strand	Strand diameter	0.847	mm
	Cu/NbTi	1.3	
	Ic @ 3T & 4.2K	> 630	A
	Filament diameter	< 30	μm
	Filament twist pitch	30	mm
Cable	NbTi strands	22	
	Transposition pitch	50	mm
	Width	6.8	mm
	Thickness	1.26	mm
Conductor	Copper channel section	39.1	mm²
	Insulated conductor section	61.1	mm²
	Nominal current	3924	A
	RRR conductor	>100	
	$\sigma_{0.2\%}$ @ 293 K	>165	MPa
	Unit length	1.05	km
	Total length	18.9	km

Each unit length of the conductor corresponds to 1 layer in the magnet. The worst condition the conductor can experiment are in the first turn of the L1 layer, MOD1, where are located the magnetic field peak B_{peak} = 2.672 T and an expected temperature of 4.7 K. At the nominal current, according to the Bottura scaling law [16] and a critical current degradation of 15% (cabling plus soldering), the expected current sharing temperature is T_{cs} = 7.15K, giving a temperature margin of 2.45K and a load-line margin of 46.1%. In terms of stability, the conductor has an enthalpy margin of 6.7 kJ·m^{-3}, providing a quite large margin respect to other detector magnets. For instance, the BaBar magnet, which is the most similar one in terms of dimensions (although with a maximum stored energy of 27MJ), has an enthalpy margin of about 3.6 kJ·m^{-3} [17].
The conductor performances are reported in Table 13:

Table 13
MARCO conductor margins

Parameter	B_{IP} = 1.5 T	B_{IP} = 1.7 T	B_{IP} = 2.0 T	Units
Current I_n	2942	3335	3924	A
T_{op}	4.7	4.7	4.7	K
B_{peak}	2.003	2.271	2.672	T
T margin	3.06	2.82	2.45	K
LL margin	59.6%	54.2%	46.1%	
I_n/I_c	17.9%	22.1%	29.3%	

The load-line of the magnet is shown in Fig. 22

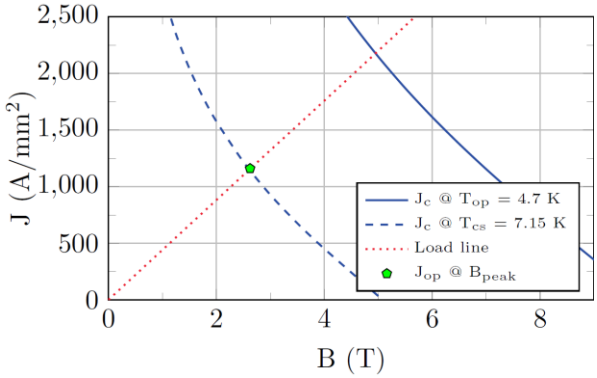

Fig. 22. Jc curve @4.7 K, load line and load line margin for the reference case study B0=2T. The working point (green rectangle) is shown, corresponding to a current sharing temperature of 7.15 K.

A complete description of the conductor and the choices made can be found in the dedicated paper [10].

VII. Mechanical Design

The mechanical design has been performed using 2D and 3D finite element models, respectively in Cast3m [18] and ANSYS [19]. A complete and detailed description of the mechanical design and analysis can be found in the related paper [20]. This paragraph is meant to summarize the efforts accomplished.

A. Material properties and coil pack homogenization

The material properties considered for the analysis are reported in [20]. For both models, a certain level of homogenization of the material properties for the coil pack has been assumed. In particular, for the 2D model the Rutherford cable inside the channel has been homogenized and simplified as rectangle, while the copper channel and the insulation has been modeled in details. For the 3D all the coil pack has been. The homogenization has been calculated using ANSYS Workbench 2023 R2 with the "Material Designer" module. The cable and coil pack homogenized mechanical properties are reported here [20].

B. 2D model assumptions

The 2D mechanical analysis was conducted in Cast3m using its magneto-static solver to calculate the Lorentz forces and its mechanical solver to analyze their impact on the magnet structure. The magnetic model includes the iron yoke, the mechanical one does not. A schematic of the mechanical model geometry is shown in Fig. 23. Each turn is modeled, with its own cable, copper channel and insulation. As contact conditions, for each module, the coil, the ground insulation and the mechanical structure are bonded together to simulate the impregnation. The coil wedges are bonded to mechanical structure and have a sliding contact with possible separation with the coils and with the inter-module wedges.

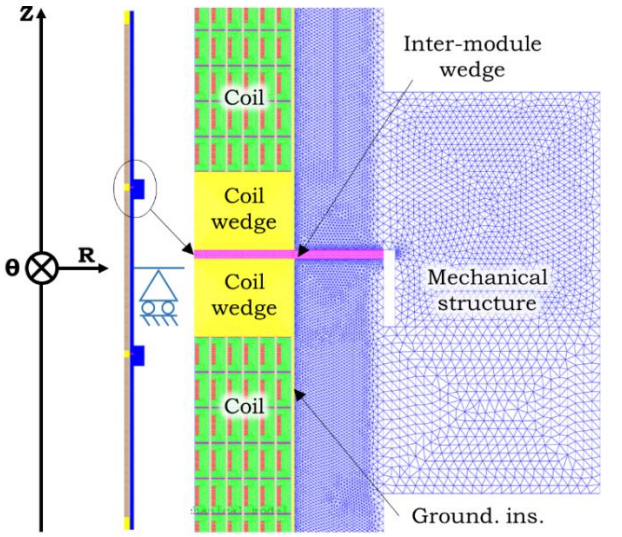

Fig. 23. 2D axisymmetric mechanical model including the coils and the mechanical structure. A zoom of one of the two areas where the 3 modules are assembled is shown. The iron yoke is not shown. Each turn is modeled, with its own cable, copper channel and insulation.

C. 3D model assumptions

The 3D mechanical analysis was conducted in ANSYS Workbench, importing the magnetic force density from the OPERA 3D model. Fig. 24 shows the geometry of the model, the tie-rods warm interfaces and the ball joints definition with their boundary conditions. The complete description can be found here [20]. Tie-rods are made from Titanium alloy Ti-6Al-4V. This material has been chosen for its high yield strength as well as for its very low thermal expansion.

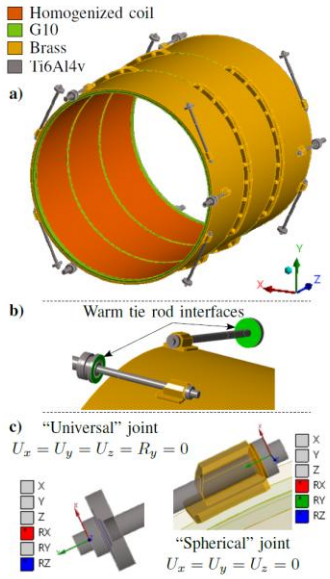

Fig. 24. a) 3D model geometry and materials. b) zoom on the tie-rods and their warm interfaces. c) the tie-rods ball joints with their boundary conditions.

D. Acceptance criteria

The acceptance criteria for the design are reported in Table 14. The main principle behind is to have an equivalent Von Mises stress and a shear stress in each component below the 2/3 of the corresponding elastic limits for each material (reference value in Table 14). For what concerns the conductor, a minimum elastic limit of 165MPa is imposed to the manufacturer. This can be easily achieved through cold-work on the copper channel, and it is below of what has been achieved for the Iseult conductor (220MPa) [14]. For the shear limit on G10, a factor of 0.4 has been assumed as acceptance criteria in order to be more conservative.

E. Results

Each component of the cold-mass fulfills the acceptance criteria of Table 14. The results related to the Von Mises peak stress and shear peak stress between the 2D and 3D models are remarkably close especially for the coils. The effect of tie-rods is notable in 3D for the mandrel, which has a VM peak stress of 280 MPa (106 MPa for the 2D). The reason is the local stress induced by the tie-rods on their pads. Due to the lack of space caused by the Barrel Yoke, the tie-rods cannot be made to compensate totally the thermal shrinkage during the cool-down, inducing a higher stress than what could be forecast. However, thanks to the fact that the mandrel is in brass, this is not an issue. A summary of the results for cool-down and energization is shown in Table 15.

TABLE 14
ACCEPTANCE CRITERIA

295 K			
Material	**Properties**	**Reference Value (MPa)**	**Acceptance criteria (MPa)**
Coil	Yield strength	165	110
	Shear strength	15	10
G10	Yield strength	257	103
	Shear strength	42	17
Brass7030	Yield strength	413	275
	Shear strength	220	88
Ti6Al4V	Yield strength	1030	687
4.5K			
Coil	Yield strength	200	133
	Shear strength	72	24
G10	Yield strength	496	198
	Shear strength	73	29
Brass7030	Yield strength	517	345
	Shear strength	264	106
Titanium alloy Ti-6Al-4V	Yield strength	1693	1129

TABLE 15
MECHANICAL RESULTS FOR COOL-DOWN AND ENERGIZATION

COOL-DOWN			
Material	**Properties**	**2DValue (MPa)**	**3D Value (MPa)**
Coil	Von Mises Peak Stress	55	70
	Shear Peak Stress RZ	14	11
G10	Von Mises Peak Stress	54	94
	Shear Peak Stress RZ	23	21
Brass7030	Von Mises Peak Stress	105	300
	Shear Peak Stress RZ		16
Ti6Al4V	Von Mises Peak Stress	NA	761
COOL DOWN + ENERGIZATION			
Coil	Von Mises Peak Stress	81	78
	Shear Peak Stress RZ	17	12
G10	Von Mises Peak Stress	84	77
	Shear Peak Stress RZ	23	18
Brass7030	Von Mises Peak Stress	106	280
	Shear Peak Stress RZ	NA	20
Ti6Al4V	Von Mises Peak Stress	NA	839

Erreur ! Source du renvoi introuvable. The results of each scenario the magnet can withstand during its life is instead reported here [20].

VIII. TRANSIENT ANALYSIS AND QUENCH PROTECTION

The transient analysis was performed for the magnet during different ramp-up and ramp-down scenarios. Since the mandrel is made from Brass 70/30, it plays a noticeable role during the transients of the magnet, in particular during ramp-up / ramp-down, fast discharge, and quench. Its magnetic behavior has been simulated using OPERA.

A. Ramp-up and ramp-down

The ramping rate (up and down) of the magnet is 1.0 A/s, which is a compromise found between ramping the magnet in approximately one hour and not overheating it at the same time due to the mandrel dissipated power. This case has been used to define the main magnetic specifications of the mandrel. Results are reported in Table 16, while the eddy current distribution can be found here [21].

TABLE 16
RAMP-UP / RAMP-DOWN RESULTS AND MAIN MAGNETIC PARAMETERS OF THE MANDREL

Parameter	**Value**	**Unit**
Ramping rate	1	A/s
Power dissipated at $t = +\infty$	3.642	W
Eddy current at $t = +\infty$	-1015.3	A
Resistance (P/I^2)	3.516	μΩ
Mutual inductance	3.570	mH
Inductance of the mandrel	2.346	μH
Coupling coefficient btw mandrel and coils	0.964	

The impact of the flanges is significant, showing that the current tends to pass through them between the adjacent modules.

B. Fast discharge

Fast discharge is the worst case for induced eddy currents in the mandrel due to the dump resistor of the circuit, the dI/dt being the highest at the beginning of the discharge. As for the quench protection, for the fast discharge case the following circuit has been considered (Fig. 25):

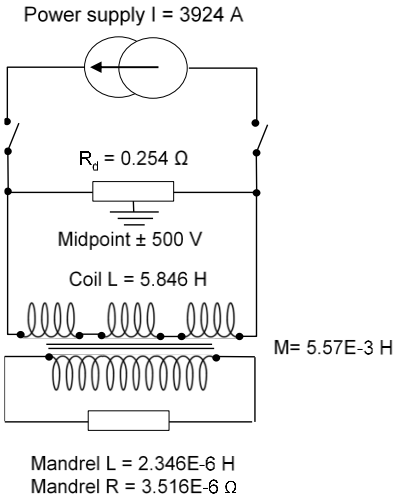

Fig. 25. Scheme of the electric circuit of the MARCO magnet.

The dump resistance R_d has been determined limiting the maximum voltage across the magnet to 1000 V. In case of fast discharge, the mandrel behaves as shown in Fig. 26.
The current in the mandrel can increase up to 165 kA in 0.3 s (Fig. 27); a vertical force of F_y = -22 kN acts on the mandrel, due to the asymmetric distribution of the eddy currents around the flanges. Such force is well below the loads that the magnet can encounter during transportation, and it is well compensated by the tie-rods. The total time needed to fast discharge the magnet is 120 s.

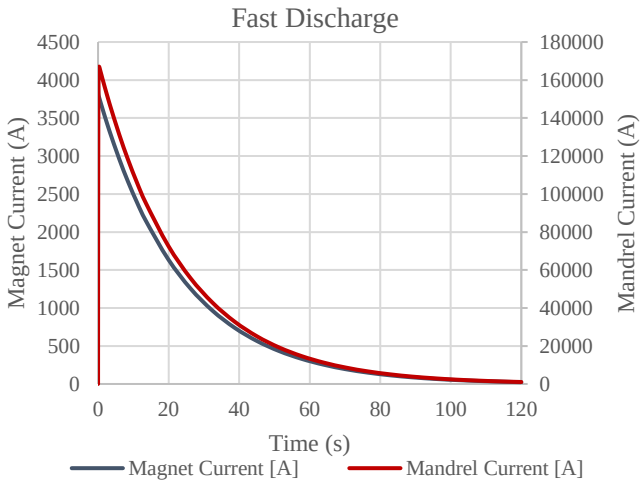

Fig. 26. Current flowing in the magnet (left vertical axis) and in the mandrel (right vertical axis) during a fast discharge.

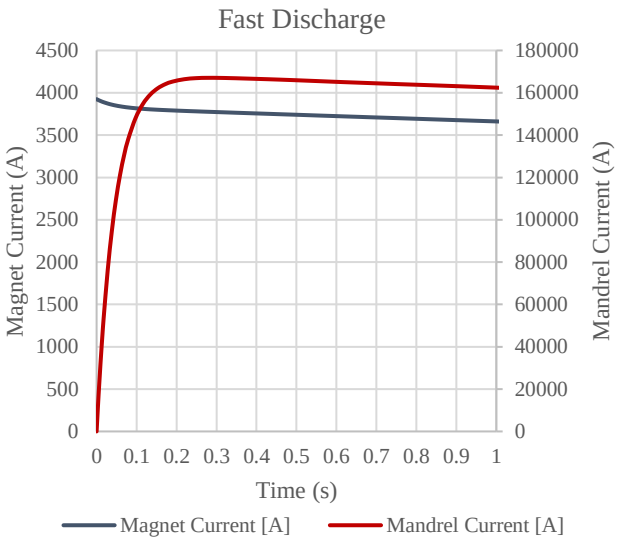

Fig. 27. Current flowing in the magnet (left vertical axis) and in the mandrel (right vertical axis) during a fast discharge, with a zoom on the first second.

C. Quench Model

Both a single coil analytical quench analysis (more conservative) and a detailed Finite Element quench analysis in COMSOL have been performed to design the quench protection. The single coil quench analysis can be found in details in [21]. In this section only the detailed FE quench analysis is described. As written, the quench analysis has been conducted using COMSOL, with a coupled 2D axisymmetric FE model and 1D model to consider the heat propagation—the first for the transverse propagation and the second for the azimuthal propagation. The logic structure of the model is shown in
Fig. 28:

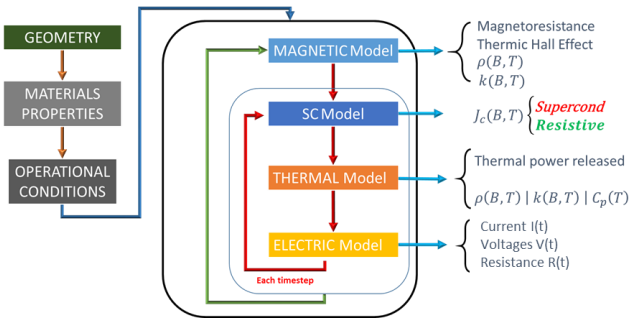

Fig. 28. Logic structure of the COMSOL quench model.

Once the geometry, material properties and operational conditions are defined, the magnetic model is solved to determine the resistivity (ρ) of each element (with respect to the magnetic field and temperature) and thermal conductivity (k). Once the magnetic field, the temperatures and materials properties are defined over the domain, the model calculates the critical current density J_c and solves the coupled thermal and electric model associated to the geometry. The model considers the full geometry of the magnet, and it defines every turn with details of the conductor. The conductor is represented by a

homogenized material (homogenized cable and copper stabilizer). The insulation is modelled separately to consider its own material properties. A representation of the geometry is shown in Fig. 29.

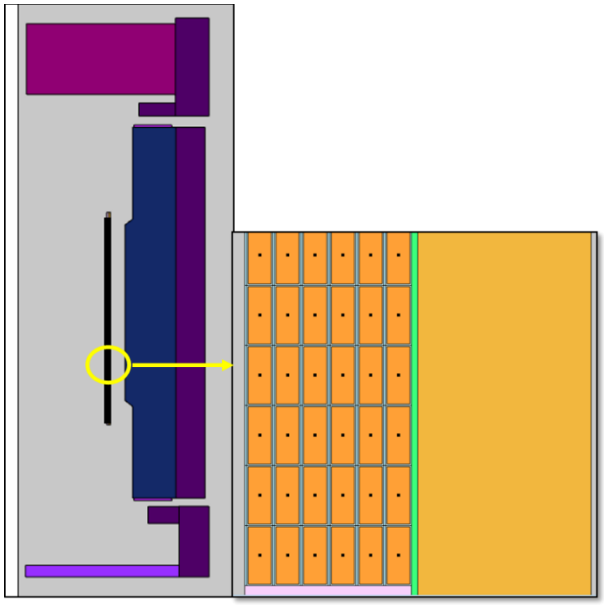

Fig. 29. Model used in COMSOL. The overall geometry includes the yoke. A zoom-in view on the area marked with the yellow circle is shown, which illustrates the turns, interlayer insulation, ground insulation, and mandrel.

The material properties are from Cryocomp [22]. The thermal hall effect and magnetoresistivity in copper are considered. The quench starts at the bottom angle of MOD1, where the peak magnetic field is located. The case studied is the one at the nominal current (3924 A) and maximum nominal temperature (4.7 K). Once the quench starts and after that the resistive tension reaches 1 V, a validation time of 1 s is needed to validate the quench and open the breakers to activate the dump resistance. The electrical circuit is shown in Fig. 25. A dump resistance of 0.254 Ω is used to limit the maximum voltage to 1000 V.

The magnetic model is solved by COMSOL with the same geometry and material properties used in the OPERA model as described in Section V. The results of two models agree with each other. Fig. 30 and Fig. 31 respectively show the magnetic field and the resistivity of each turn of MOD1, presented here as an example.

The superconducting model calculates at every turn to determine if the conductor is in the superconductive state, in the resistive state, or in the current sharing state. It uses the Bottura fit parameters used to design the MARCO conductor to calculate the critical current density in the cable. A simple model of current redistribution is considered: if the critical current $I_c \geq 0$ and $I_c < I(t)$, where I(t) is the current flowing through the cable, the ohmic power dissipated is smoothed by an inverse sigmoid.

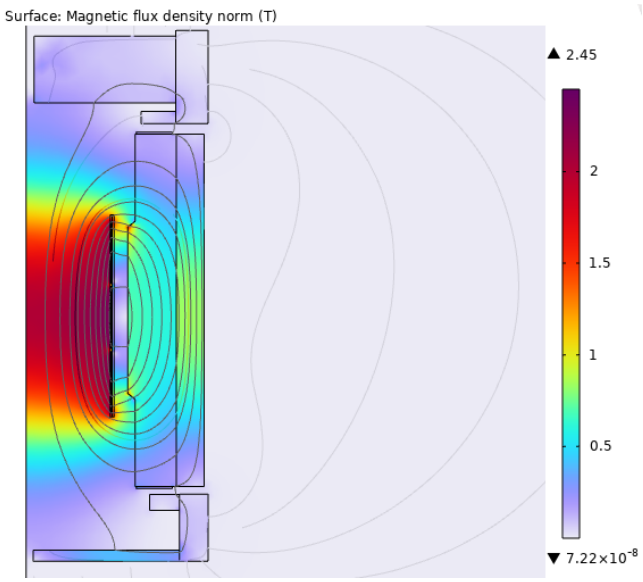

Fig. 30. Magnetic field map computed in the COMSOL model.

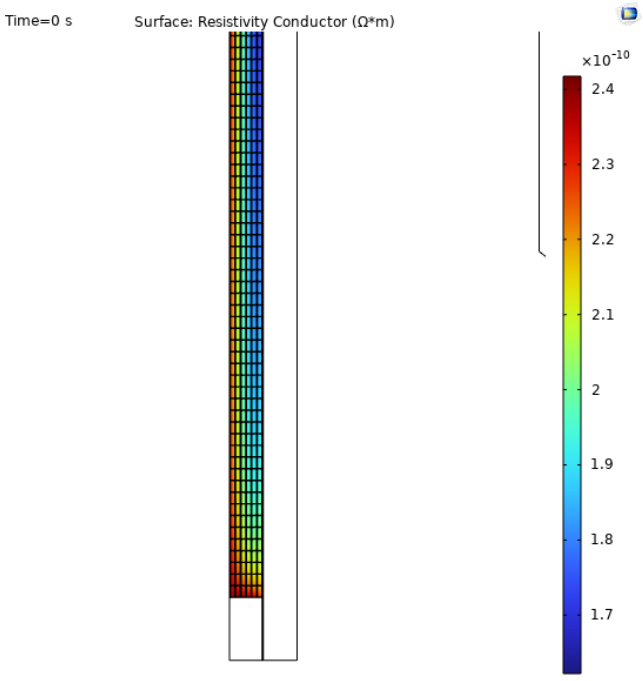

Fig. 31. Conductor resistivity at nominal current for MOD1.

The thermal model solves the heat transfer equations in 2D associated with every node of the model and the 1D propagation along the length of the conductor according to the computed azimuthal quench velocity. The ohmic power releases at every turn when quenched is considered starting at the node in the center of the conductor geometry.

The electrical model calculates the resistivity and voltage associated with every turn and the eddy currents induced in the mandrel during the quench current decay.

D. Quench Analysis for the nominal case scenario

In the nominal case scenario, the magnet is protected by the dump resistance R_d. Due to the high inductance, the current decay is very slow and it takes 65 s to reach less than 1% of the

original current in the magnet. The time constant of the quench circuit is 20.31 s.
Fig. 32 shows the current decay in the coils and the eddy current in the mandrel. Thanks to the good magnetic coupling between the coils and the mandrel, the mandrel is subjected to the high eddy current, which generates the quench-back in the coils (Fig. 33).

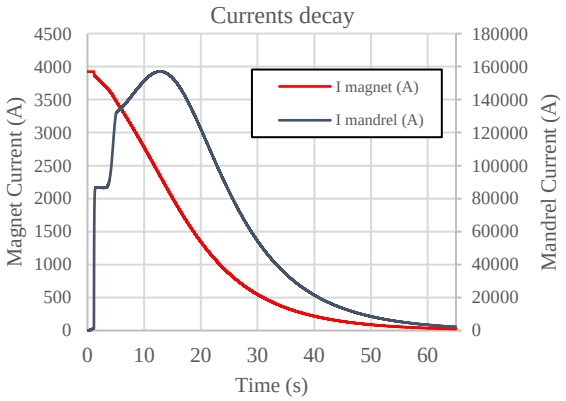

Fig. 32. Current decay in the coils (red line, left axis) and in the mandrel (blue line, right axis) as a function of time.

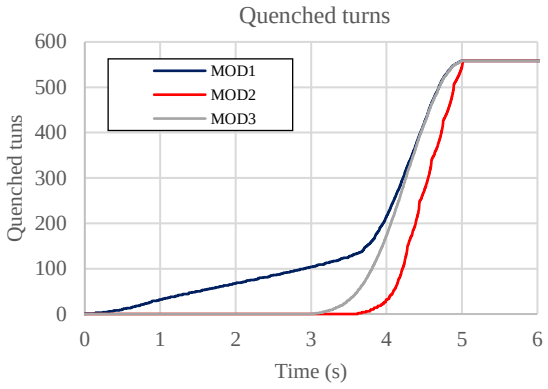

Fig. 33. Number of quenched turns as a function of time in the three different modules. The quench-back induced by the mandrel can be easily seen since the quench propagation velocity changes from MOD1 to MOD2 and MOD3.

The resistive coils voltage profile during quench shows no issue; the maximum voltages inside the coils are around 1000 V, the acceptable criterion defined for the magnet (Fig. 34).

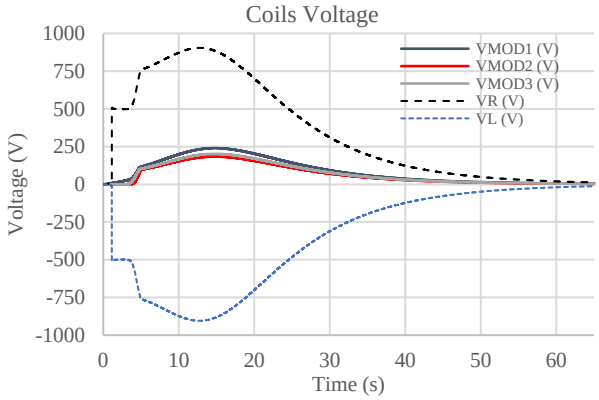

Fig. 34. Resistive coil voltage as a function of time for the three modules (VMOD1, VMOD2, VMOD3), the resistive voltage profile (VR) and the inductive voltage profile (VL) of the overall circuit (magnet plus Rdump).

The total power dissipated in the circuit is shown in Fig. 35. The dump resistance has a peak power of 3.8 MW; the coils, 1.5 MW; the mandrel, 86 kW.

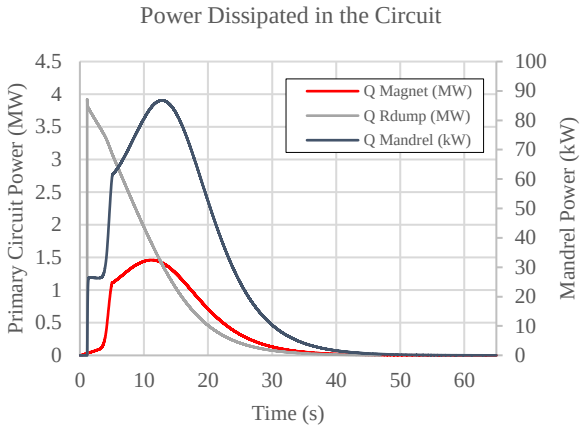

Fig. 35. Power dissipated in the primary circuit (magnet – red line – and dump resistance – grey line) on the left axis, in the mandrel (blue line) on the right axis.

The maximum temperature (hotspot) reaches during quench is 96 K (Fig. 36), showing no issue for the structural integrity of the magnet. The hotspot is located at the quench starting point (Fig. 37).

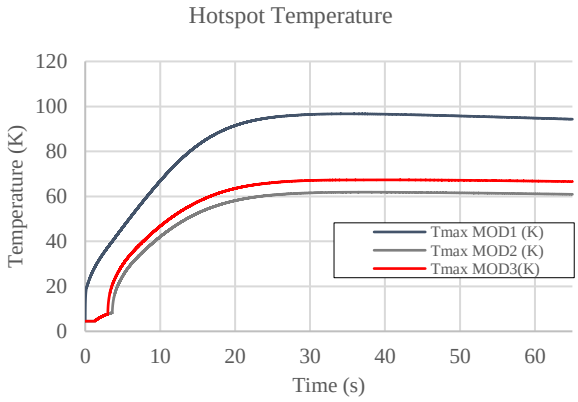

Fig. 36. Hotspot temperature in the three modules of the magnet. Since the quench starts in MOD1 (blue line), the corresponding hotspot temperature is higher than the ones in the other two modules. The difference between MOD2 and MOD3 (both quench thanks to the quench-back by the mandrel) in maximum temperature is due to the different magnetoresistance the two modules have.

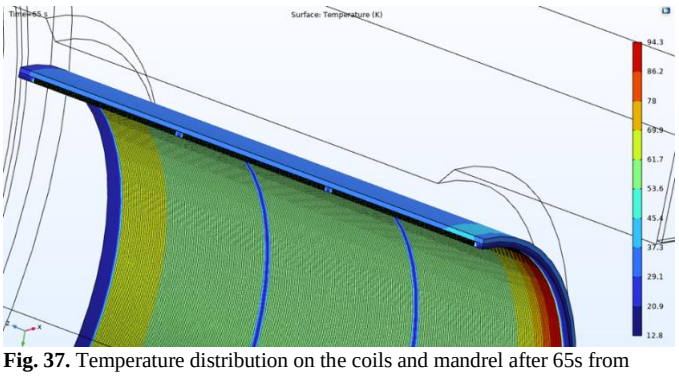

Fig. 37. Temperature distribution on the coils and mandrel after 65s from quench.

IX. Cryogenics Design

The MARCO magnet is a conduction-cooled magnet and it is indirectly cooled using the cooling tubes on the outside of the brass mandrel. The internal cryogenic system of the Marco solenoid for EIC experiment involves a cold mass, which consists of a mandrel and coils with two 28-tube exchangers of the thermosiphon soldered on the mandrel, a phase separator on top used also as a storage tank of liquid helium at 4.55 K, and one cryogenic chimney that holds the helium vapor cooled current leads and connect the phase separator to the cold mass. The solenoid is equipped with 5 cold valves with warm actuators and 3 warm valves (Table 17). It also has a thermal shield to insulate the parts at 4.5 K; the thermal shield is cooled by helium gas between 45 K and 65 K. The internal cryogenic system is connected to the BNL refrigeration supply through flexible lines. The cryogenics flow chart is shown in Fig. 38, while the piping schematics of thermosiphon is shown in Fig. 39.

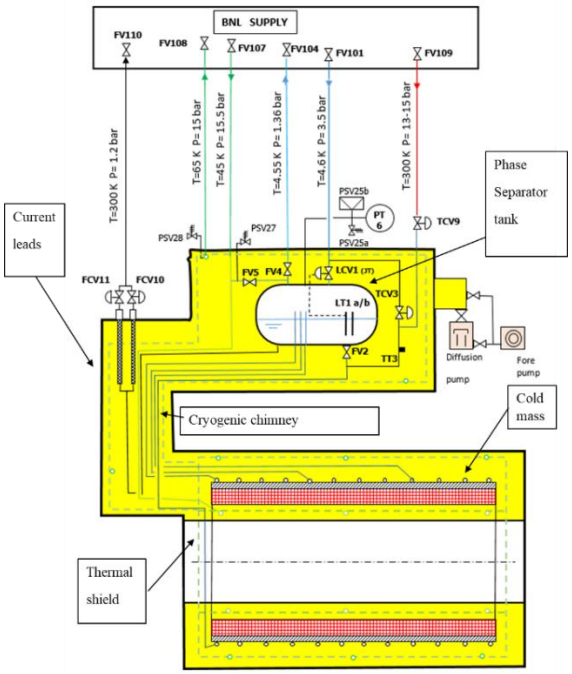

Fig. 38. Cryogenics flowchart of the MARCO solenoid.

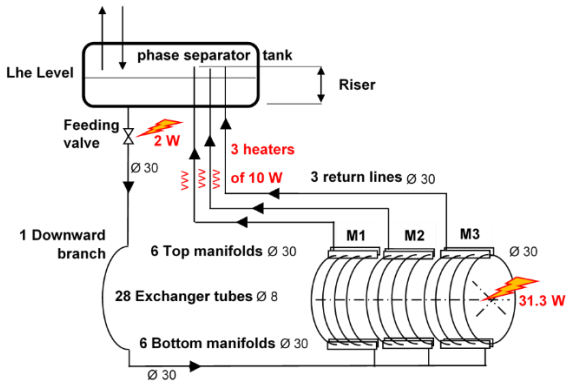

Fig. 39. Schematics of the thermosiphon system.

Table 17
CRYOGENICS VALVES AND THEIR DESCRIPTION

Name	Description
FV101	BNL supercritical helium shut-off valve
FV104	BNL vapor helium shut-off valve
FV107	BNL inlet helium for thermal shield shut-off valve
FV108	BNL outlet helium for thermal shield shut-off valve
FV109	BNL inlet warm helium for cool-down shut-off valve
FCV110	BNL outlet helium for current leads shut-off valve
PSV27	Inlet helium for thermal shield safety valve
PSV28	Outlet helium for thermal shield safety valve
PSV25a	Relief valve for the phase separator tank at 4.5 bar abs. (quench)
PSV25b	Burst disc for the phase separator tank at 6 bar abs. (vacuum loss)
PT6	Pressure measurement of the phase separator tank
FCV10	Flow control valve for current lead a
FCV11	Flow control valve for current lead b
TCV9	Warm temperature control valve for cool-down
TCV3	Cold temperature control valve for cool-down
TT3	Temperature of the mixed gas coming from TCV3 and TCV9 for the cool-down
FV2	Feeding shut-off valve of the thermosiphon
FV4	Vapor helium shut-off valve
FV5	Bypass shut-off valve for vapor helium into the shield in case of refrigerator shut-off
LCV1	Level control valve for the liquid helium in the tank (Joule Thomson valve)
LT1a/b	Liquid helium measurement in the tank with spare

A. The thermosiphon

The solenoid is cooled by a two-phase flow helium thermosiphon. Twenty-eight exchanger tubes (2x5 tubes for module 1, 2x4 tubes for module 2, 2x5 tubes for module 3) are soldered on the brass mandrel. Liquid helium is stored in the phase separator tank and flows through valve FV2 down in the downward branch to supply 6 distributors (bottom manifolds). This flow of helium is heated up in the exchanger tubes, collected by 6 collectors (top manifolds), and goes back to the tank through 3 return lines. Three heaters (10 W maximum each) are placed on the return lines in case that there is not sufficient heat load on the cold mass. The return lines go back in the phase separator tank at a higher level than the feeding line which is connected directly to the bottom of the tank, the difference of height is the riser. These risers make the return two phase flows pour out the return tubes above the liquid surface area in the phase separator tank. When the level of liquid is zero the tank is empty, when it is nominal, it is equal to 0.3 m whereas the risers are 0.4 m high.

There are two thermosiphon piping systems. One is primary and one is spare. If the primary has a leak, it is possible to use the spare one by disconnecting the primary piping in the vacuum vessel of the phase separator tank and connecting the spare piping. The heat exchanger tubes are made of copper. They have an outer form of a square (14 mm x 14 mm) and an inner diameter of 8 mm. They are soft soldered onto the brass mandrel. At their extremities, stainless steel junction tubes (jumpers) are brazed inside the copper tubes, and these junctions is welded to the stainless-steel manifolds. Fig. 40 and Fig. 41 show in details how the thermosiphon is designed.

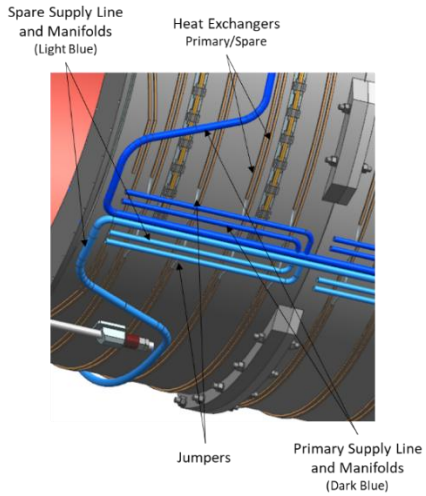

Fig. 40. Primary and spare tubes of the thermosiphon heat exchanger.

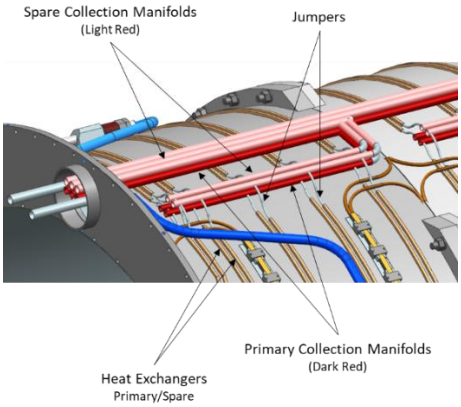

Fig. 41. Primary and spare piping on top of the mandrel.

The outlet pressure of the return lines in the phase separator tank must be the same as the pressure inside the tank, defining thus the mass-flow rate and then the vapor quality. The case under consideration is the shut-down of the refrigerator when the liquid helium level is dropping in the phase separator tank. The limit is where the level is equal to zero and thus the tank is empty. This is the limiting case for the thermosiphon because the differential height between the downward branch and the return lines (upward branch) is maximum and equal to the riser (0.4 m). The riser is needed to ensure that the two-phase flow goes back to the phase separator tank above the liquid helium surface in any case. The diameters (Ø8 mm) of the exchanger tubes of the supply and return lines, and the diameter (Ø30 mm of manifolds) have been chosen to lower the frictional pressure drop. The main pressure drop is in the riser due to the gravity. In addition, the manifolds are almost isobaric as their pressure drop is less than 1 Pa. Several heat loads scenario has been considered for the thermosiphon, according to the possible heat loads present inside the cryostat (see Table 19). For any of these cases, the vapor quality is below 10% and the speed of the He in the return line is always greater than 0.1 m/s, assuring the proper operation of the thermosiphon (Table 18).

TABLE 18
THERMOSIPHON LOAD CASES

Case	Value	Unit
Cold mass heat load at zero current	**25**	**W**
Heaters (off)	0	W
Total mass flow rate	25.4	g/s
Vapor quality	6 %	
Flow speed in the return lines	0.13	m/s
Cold mass heat load during ramp-up/down	**30**	**W**
Heaters (off)	0	W
Total mass flow rate	29.1	g/s
Vapor quality	6.2 %	
Flow speed in the return lines	0.14	m/s
Cold mass low level heat load	**10**	**W**
Heaters (on)	20	W
Total mass flow rate	18.3	g/s
Vapor quality	9.8 %	
Flow speed in the return lines	0.10	m/s
Cold mass high level heat load	**60**	**W**
Heaters (off)	0	W
Total mass flow rate	45.6	g/s
Vapor quality	9.8 %	
Flow speed in the return lines	0.24	m/s

B. The thermal shield

The thermal shield of the cold mass is made of 12 internal panels (4 panels per module) and 12 external panels (4 panels per module), and end plates. It is made of Al 3003 with a thickness of 5 mm. The tube, which connects the BNL flexible supply line and the thermal shield piping, has an inner diameter of 10 mm and an outer square form of 14 mm x 14 mm. This tube passes through the phase separator vacuum vessel and the cryogenic chimney without cooling any surface; it goes directly to the inner part of the cold mass thermal shield and supplies, in parallel, the left circuit and the right circuit. The left and right external shields are then cooled afterwards. The end plates are indirectly cooled by connecting with them. The two half flows are joined together at the inlet of the cryogenic chimney and then cools the thermal shield in the cryogenic chimney. Like the thermosiphon system, there are two cooling circuits for the thermal shield. One is the primary and the other is the spare.

C. The helium phase separator

The helium phase separator is on top of the detector, embedded in the iron and connected to the magnet assembly through the cryogenic chimney (Fig. 42).

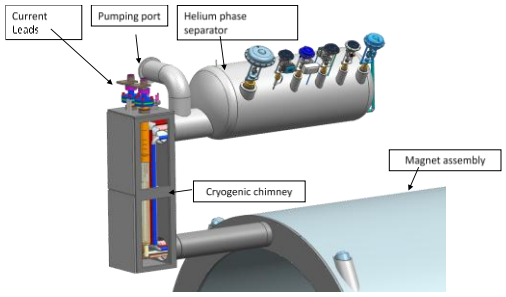

Fig. 42. Helium phase separator and cryogenic chimney overview.

In addition to the cryogenic lines, the cryogenic chimney also houses the helium vapor cooled current leads (AMI L-5000A [23]). A vacuum pumping port is located between the cryogenic chimney and the phase separator vacuum vessel. The total volume of the inner helium vessel is 284 L; the liquid helium buffer used in normal operation is 110 L which is the volume of liquid needed to ramp down the current at 1 A/s in case of a refrigerator shut-down the liquid helium level in the tank is then 0.3 m. The set pressure of the burst disc is 6 bar. The protection against overpressure is studied according to European regulations, for the helium circuits including the phase separator (inner vessel): EN21013-3 and for the vacuum vessel (outer vessel): EN 13458-2. The European regulations are stricter than the US regulations (ASME BPVC VIII Div.1/2). Applying them to the design will allow to test the magnet also in Europe, in case the manufacturer will be European.

D. Heat loads

The cryogenic heat loads are calculated for all the components of the cryogenic system and they are listed in Table 19:

TABLE 19
HEAT LOADS SUMMARY

Heat load source	**Value**	**Unit**
Tie-rods for the cold mass @4.5K	3.68	W
Tie-rods for the cold mass @65K	79.2	W
Tie-rods for the phase separator tank @4.5K	0.48	W
Tie-rods for the phase separator tank @65K	12.8	W
Cold valve LCV1 @ 4.5K	0.31	W
Cold valve FV2 @ 65K (@4.5K)	10 / (3)	W
Cold valve TCV3 @ 4.5K	0.36	W
Cold valve FV4 @ 65K (@4.5K)	5 / (1.4)	W
Cold valve FV5 @4.5K	0.31	W
Bellows for valve PSV25a / burn disc PSV25b @4.5K	0.19	W
Flexible lines @ 4.5K	2	W
Thermal shield supports @ 55K	32	W
Heat radiation (radiation flux = 0.3W/m^2) @4.5K	23.1	W
Heat radiation (radiation flux = 5 W/m^2) @65K	420	W
Conductor junctions (1.0nΩ each)	0.32	W
Hysteresis from NbTi filaments	0.8	W
Eddy current in strand copper (ramp-up/down)	0.2	W
Eddy current in the mandrel (ramp-up/down)	3.7	W
Helium vapor cooled current leads	12	W

The heat load budgets at 4.5 K and 65 K are outlined as follows (Table 20).

TABLE 20
HEAT LOADS BUDGET

4.5 K		
Element	**Value**	**Unit**
Cold mass at zero current	25	W
Cold mass at ramping up/down (1 A/s)	30	W
Phase separator tank	10.2	W
Current leads	12	W
Margin	5	W
45 K - 65 K (loads on thermal shields)		
Thermal radiation	420	W
Support conduction	32	W
Thermal intercept	107	W
Margin	61	W

The maximum heat load (when ramping up the current) at 4.5 K is 57 W. The total heat load budget on the thermal shield is 600 W. The impact of the heat loads on the temperature of the cold mass can be found here [24]

X. INSTRUMENTATION & CONTROL

In order to operate and monitor the MARCO solenoid an extensive instrumentation plan have been conceived. The instrumentation covers the electrical measurements, the cryogenics data measurements as well as the mechanical ones. The electrical measurements gather the voltage measurements and the current measurements. The cryogenics ones collect the temperature data, the pressure, the liquid helium level, the He mass flows and the vacuum level. Finally, the mechanical measurements concern especially the tie-rods whose stress is monitored during all the magnet life.

A. Voltage Taps

The electrical instrumentation scheme has been done based on the magnet protection analysis and choices. As the magnet will be protected by a Main Safety System (MSS) the voltage will be monitored for each coil segment with a redundancy. The quench detector will be made by making the difference between two segments of the coil having the same inductance, allowing to remove the inductive voltage and read only the resistive voltage. This will permit the MSS to detect the transition time and protect the magnet by opening the contactor to discharge the magnet on the dump resistor. With the redundancy, 50 voltage taps shall be positioned in the magnet giving 25 differences of potential to measure and send to the MSS and acquisition system. These measured values can be combined in 16 quench detectors with 12 for the coils, 2 for the current leads and 2 for the busbars (one per current lead and one per busbar). For the coils the voltage threshold has been set to 0.1 V to 1 V in the simulation with at least one second of validation time. For the busbars, the voltage threshold is smaller and have been set to 10 mV with a validation time of 10 ms. Finally, the voltage threshold of the current leads shall be smaller than the maximum operating voltage in the current leads. Two DCCTs shall be position to monitor and regulate the current. The first one between the power supply and the contactor shall be used for the power supply regulation while the second one be-tween the coil and the dump resistor will be used to monitor the current in case of quench or contactor opening.

B. Cryogenics instrumentation

For the cryogenic instrumentation plan, different type of sensors will be used. The first ones are the temperature sensors whose are divided in two types, the PT100 for all the temperature above 50 K i.e., for the thermal screen and the CERNOX® sensors used for all the 4.5 K measurements. For the PT100, 10 will be placed on the thermal screen while 6 will be placed on the current leads. Concerning the CERNOX, 12 will be distributed all over the magnet and shell and 6 distributed between the bus-bars, the phase separator, the thermosiphon inlet and outlet. Completing the thermal sensors flow meters (2 for the current leads, 2 to 4 for the thermosiphons inlet and outlet and 2 for the 50 K shield inlet and outlet) will

be used to monitor the cryogenic operation as well as 2 liquid helium level gauges, 2 manometers and 2 vacuum gages.

C. Mechanical sensors

To monitor the tie-rods preload during the magnet assembly in its cryostat, the transport, the magnet cool down and energization, it is planned to use load cells placed at the end of each tie-rods. These load cells shall be dimensioned adequately pending the stress analyses made during the design phase.

XI. Conclusion

MARCO will be a unique solenoid for detector magnets: although it will use a Rutherford in Copper Channel Conductor (RICC) and a mandrel in brass 70/30, it will meet the stringent criterion on the transparency typical of every detector magnet. Today, the detailed design is completed and the risk assessment has been detailed [25]; the conductor first samples are in production and its fabrication is forecast to start in the next year.

Acknowledgment

This material is based upon work supported by the U.S. Department of Energy, Office of Science, Office of Nuclear Physics under contract DE-AC05-06OR23177. The authors would like to thank all of the members of BNL, CEA Saclay, and JLab teams who have contributed to this work.

References

[1] A. Accardi and al., "Electron Ion Collider: The Next QCD Frontier - Understanding the glue that binds us all," BNL, 2014.

[2] ePIC Collaboration, "ePIC website," [Online]. Available: https://www.epic-eic.org/. [Accessed 1 September 2024].

[3] S. della Torre, "The Electron-Ion Collider and the ePIC experiment," *IL NUOVO CIMENTO*, vol. 47 C, no. 144, 2024.

[4] Brookhaven National Laboratory, "EIC," 2024. [Online]. Available: https://www.bnl.gov/eic/goals.php.

[5] ePIC Collaboration, "ePIC Wiki," 2024. [Online]. Available: https://wiki.bnl.gov/EPIC/index.php?title=Main_Page. [Accessed 01 September 2024].

[6] R. Bell and al., "The BaBar superconducting coil: design, construction and test," *Nuclear Physics B*, pp. 559-564, 1999.

[7] ATLAS Collaboration, "ATLAS central solenoid : Technical Design Report," CERN, Geneve, 1997.

[8] CMS Collaboration, "The Magnet Project Technical Design," CERN, Gèneve, 1997.

[9] A. Yamamoto and al., "The ATLAS central solenoid," *Nuclear Instruments and Methods in Physics Research*, pp. 53-74, 2007.

[10] R. Fast, J. Grimson and R. Kephart, "Design report for an indirectly cooled 3-m diameter superconducting solenoid for the Fermilab Collider Detector Facility," Fermi National Accelerator Lab, 1982.

[11] F. Stacchi and al., "Rutherford-In-Copper-Channel Conductor for the MARCO Solenoidal Detector Magnet," *to be published.*

[12] P. D. G. LBL, "The Review of Particle Physics," LBL, 2022. [Online]. Available: https://pdg.lbl.gov/2022/.

[13] Dassault Systems, "OPERA," Dassault Systems, 2024. [Online]. Available: https://www.3ds.com/fr/produits-et-services/simulia/produits/opera/.

[14] H. Kanithi and al., "Production Results of 11.75 Tesla Iseult/INUMAC MRI Conductor at Luvata," *IEEE TRANSACTIONS ON APPLIED SUPERCONDUCTIVITY*, vol. 24, no. 3, p. 6000504, 2014.

[15] C. Berriaud and al., "Conductor R&D for the Iseult/INUMAC whole body 11.7 T MRI magnet," *IEEE Trans. Appl. Supercond*, vol. 20, no. 3, pp. 1408-1411, 2010.

[16] L. Quettier and al., "Commissioning Completion of the Iseult Whole Body 11.7 T MRI System," *IEEE Transaction on Applied Superconductivity*, vol. 30, no. 4, 2020.

[17] L. Bottura, "A Practical Fit for the Critical Surface of NbTi," *IEEE Transactions on Applied Superconductivity*, vol. 10, no. 1, pp. 1054-1057, 2000.

[18] T. O'Connor and al., "Design and Testing of the 1.5 T Superconducting Solenoid for the BaBar Detector at PEP-II in SLAC," *IEEE TRANSACTIONS ON APPLIED SUPERCONDUCTIVITY*, vol. 9, no. 2, p. 847, 1999.

[19] CEA, "CAST3M is a Trademark of CEA/Saclay France [Online].," CEA, [Online]. Available: www-cast3m.cea.fr..

[20] ANSYS, "ANSYS," ANSYS, [Online]. Available: https://www.ansys.com/.

[21] H. Reymond, M. Segreti and al, "Mechanical design of the MARCO solenoid detector magnet," *to be published.*

[22] P. Ghoshal and et, "Quench Analysis of EIC Central Detector (ePIC) Solenoid Magnet (MARCO)," *IEEE*, vol. to be published.

[23] R. S. a. V. A. P. Eckels, *"CryoComp program",* Eckels Engineering Inc. , 1993.

[24] American Magnetics, "American magnetics," American magnetics, October 2024. [Online]. Available: https://www.americanmagnetics.com/currentleads.php.

[25] S. Gopinath, J. Lottin and al, "Cryogenic Design and Thermal Analysis of EIC Central Detector (ePIC) Solenoid Magnet (MARCO)," *IEEE Transaction on Applied Superconductivty*, to be published.

[26] P. Ghoshal and al., "Risk Assessment of EIC Central Detector (ePIC) Solenoid Magnet (MARCO)," *IEEE Transaction on Applied Superconductivity*, to be published.

[27] M. N. Wilson, Superconducting Magnets, Oxford University Press, 1983.